COMPARATIVE PERFORMANCE OF PEM ELECTROLYZER: STATIONARY VS DYNAMIC MODE

Jordan Iliev[1], Dimitar Boychev[1], Galin Borisov[1], Vladimir Dimitrov[2], Evelina Slavcheva[1]

[1]*Institute of Electrochemistry and Energy Systems "Academician Evgeni Budevski" Bulgarian Academy of Sciences, Acad. Georgi Bonchev St., Bl. 10, Sofia 1113, Bulgaria joiliev@iees.bas.bg (J.I.), dboychev@iees.bas.bg (D.B.), gal.rusev@iees.bas.bg (G.R.) eslavcheva@iees.bas.bg (E.S.)*

[2]*Technical University of Sofia, 8 Kliment Ohridski Blvd., Bl. 1, Sofia 1797, Bulgaria dimitrov@tu-sofia.bg (V.D.)*

Received 05 February 2025
Accepted 19 April 2025
DOI: 10.59957/jctm.v60.i5.2025.12

ABSTRACT

This study investigates the performance of a commercial PEM (proton exchange membrane) electrolysis cell, with a working area of 16 cm^2 and catalyst loading of 2 mg cm^{-2} of IrRuOx on the anode, and 0.5 mg cm^{-2} of 60 % PtC and 0.25 mg cm^{-2} of PtB on the cathode side, under constant and dynamic conditions to identify optimal operating modes for practical use. For this purpose, a custom programmable proportional-integrated (PI) direct current (DC) regulator and a pulse-width-modulation (PWM) frequency generator were developed to provide stationary and dynamic modes, functioning as a single system with integrated data logging for cell voltage, temperature, and pressure sensors via a C# program. Experiments confirmed that square wave pulse loading at 1 Hz with 50 % duty cycle provides increased efficiency by reducing the cell voltage compared to a continuous DC operation.

Keywords: constant power profile, dynamic power profile, management system, PEM electrolysis cell, pulse electrolysis.

INTRODUCTION

Growing energy demand resource scarcity, and environmental impacts drive the shift toward cleaner energy systems. Hydrogen technologies, particularly electrolysers with polymer electrolyte membrane (PEMWE), offer efficient, low impact energy storage [1].

Hydrogen production through water electrolysis, especially with renewable energy sources like solar energy, is an efficient way to obtain pure hydrogen. While alkaline electrolysers are still the most broadly used, they face drawbacks such as lower hydrogen purity, corrosion, and high-power consumption. The PEM electrolysers (PEMWE) as a newer technology offer several key advantages: higher efficiency, higher hydrogen purity and production rates, compact design, reduced power consumption, high pressure operation, environmental safety, easier maintenance, and compatibility with renewable energy sources and fuel cells [2].

In a PEM electrolysis cell, electrical energy splits de-ionized water intro hydrogen and oxygen, converting it to chemical energy. The main energy converting element of the electrolysis cell is the membrane electrode assembly (MEA) which consists of two electrodes attached on both sides of a polymer electrolyte membrane (PEM). Both electrodes, anode and cathode, where the partial reaction of oxygen evolution (OER) and hydrogen evolution (HER) occur have multilayered structure including gas diffusion layer distributing the reactant water and the produced gases, and catalytic layer facilitating the partial electrode reactions. The most used catalysts are Ir, Ru and their oxides for the anode as well as Pt and its alloys for the cathode. The electrolyte is a solid proton exchange membrane which enables the proton transfer and prevents mixing of the produced hydrogen

and oxygen gases. The reactant water is oxidized at the anode. The produced hydrogen ions are transported across the proton conductive membrane and hydrogen is generated at the cathode [3].

Various parameters impact the PEMWE performance, with each potentially having positive and negative effects, requiring careful balance for peak performance. For instance, parameters like membrane thickness affect both gas crossover and ohmic overpotential. The thicker membranes diminish the hydrogen crossover (positive effect), while on the other hand increase the ohmic resistance, thus decreasing the system efficiency. The analysis of the electrolyser operation can be conducted through experimental, analytical, or numerical methods. Numerical modelling, though complex, allows for evaluating key parameters- such as reaction rate, temperature, pressure, reactant concentration, current density, etc.- by solving electrochemical kinetic equations [2]. While the thermodynamics of water electrolysis is well studied, optimizations of PEMWE parameters using algorithms remains limited [3, 4]. The Taguchi method lowers computational and experimental costs by identifying influence of key parameters on performance. Notably, the anode exchange current density has a major effect on the MEA performance, while the water content and pressure at the anode side of the cell have minimal effects [5].

The controversial effect of numerous factors on PEMWE efficiency applies also to the integration with renewable energy sources which are known for their intermittent nature [6, 7]. Mitigating challenges like load fluctuation, on/off cycles, and power quality issues, contribute to the optimization of PEM electrolysers for sustainable hydrogen production [8].

Durability and degradation are critical factors for optimizing PEM electrolysis cells, and understanding these aspects is essential for improving their long-term performance. It is important to identify the key factors influencing degradation, such as current densities, contamination, and membrane activation protocols, while also exploring the role of standardized testing protocols in ensuring consistent results [9]. Addressing passivation issues in components like bipolar plates and porous transport layer (PTL) also contribute to the development of strategies for enhancing the durability of PEM electrolysis cells under both continuous and dynamic operational conditions [10].

The research presented herein, examines the effects of dynamic power on PEMWE operation switching between on/off cycles to obtain detailed information about the effects of different fluctuation patterns on cell performance [9]. The study is inspired by the work in [10].

The study aim is to compare the operation of a PEMWE single cell under constant and variable power profiles. To achieve this, an electronic system that simulates dynamic conditions by directly implementing laboratory-optimized operating modes into the system's programming was developed.

The main idea of the article aims to demonstrate how an automated control system for an electrolysis cell can be developed and implemented, allowing electrochemists to accurately interpret experimental results. Automated electronic control of processes in industry (electrochemistry) makes them more precise, safe, and efficient. Through specialized controllers and software, key parameters can be monitored in real time, allowing quick response to any irregularities. These systems can be upgraded based on electrochemists' needs. The result is higher quality, fewer errors, and a safer working environment.

EXPERIMNTAL

The experimental section presents the main blocks of the developed system and its modes of operation.

Device setup

The main goal of the designed electronic system is to act as a programmable load to the tested electrolysis cell, as shown in Fig. 1. To be able to operate properly it need to set the current density and measure cell voltage, temperature, and pressure of the electrolysis cell. The measured values are discretized with the analog-to-digital converter (ADC) of a microcontroller (MCU). The measured values are used in the developed algorithm to generate the required current reference waveform. This waveform is converted to analog signal and acts as an input to a current source generator. Detailed information regarding the possible modes of operation of the system are given below.

Constant current profile

To achieve our goal, a continuously acting, series-type PI current regulator has been designed relying on a microprocessor control system from the PIC family

(PIC16F1829) which handles logic and arithmetic functions [11]. This system allows for adjustment of current density in stationary mode. Additionally, a relay protection mechanism has been integrated to cut off power supply upon detecting deviations from the set boundary operating parameters (cell voltage, temperature, and pressure). A block and schematic diagram of the system are shown in Fig. 1 and Fig. 2, respectively.

The individual blocks are presented in Fig. 2.

Task generator and digital-to-analog converter (DAC)

The current regulator is composed of two main functional modules - a processor and a DAC. The "reference assignment" is coded in 5-bit format and stored in the non-volatile EEPROM memory of the microprocessor. This ensures that after turning down the entire setup and then turning on again, any previous settings that have been made will be automatically loaded into each variable accordingly. The DAC is embedded in the single-package MCU.

Regulator

In Eq. (1), a comparison is made between the regulated quantity - the current through the electrolysis cell I_t and the control signal - U_m, where conversion factor k_t is 1:

$$I_t = K_t . U_m \tag{1}$$

Relay protection

A thermal resistor Pt1000 (RTD) is used to measure the temperature. It is connected in a Wheatstone bridge and connected to a differential amplifier (Fig. 3).

Calibration of Pt1000 is performed based on the RTD's temperature-resistance correspondence table. Supply voltage should be set to 3 V to minimize heat dissipation losses i.e. thermal losses. Relay protection is configured to activate at 80°C.

The differential amplifier is used based on OP07 operational amplifier. Its output voltage reaches 421 mV at 0°C, while at 80°C, the measured output is 2.24 V, and for 100°C - 2.6 V.

The ADC module of the PIC16F1829 MCU is 10-bit, providing 1023 discrete steps. A 5 V supply with no dedicated reference source is used, yielding a voltage step size of 5 V / 1023 ≈ 4.88 mV, which corresponds to 86 steps, while at 2.6 V it corresponds to 533 steps. Outside the range of 86 and 533, the sensor signals an error. The step difference (Δ) is calculated in Eq. (2):

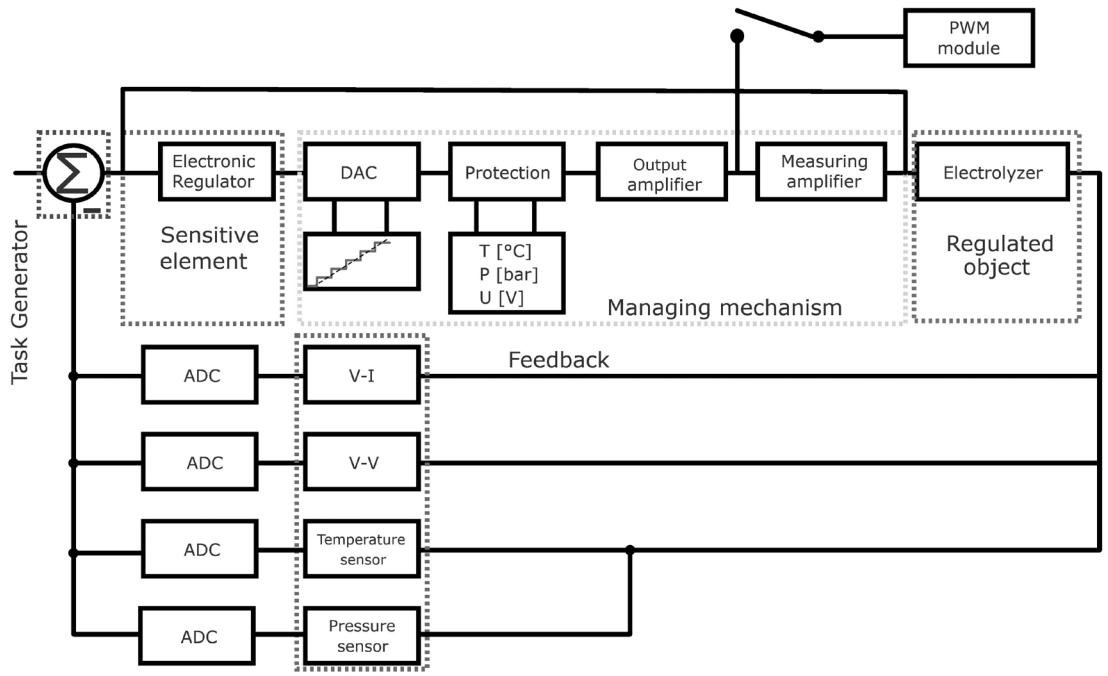

Fig. 1. Block diagram of a system for automatic regulation of the electrolyzer.

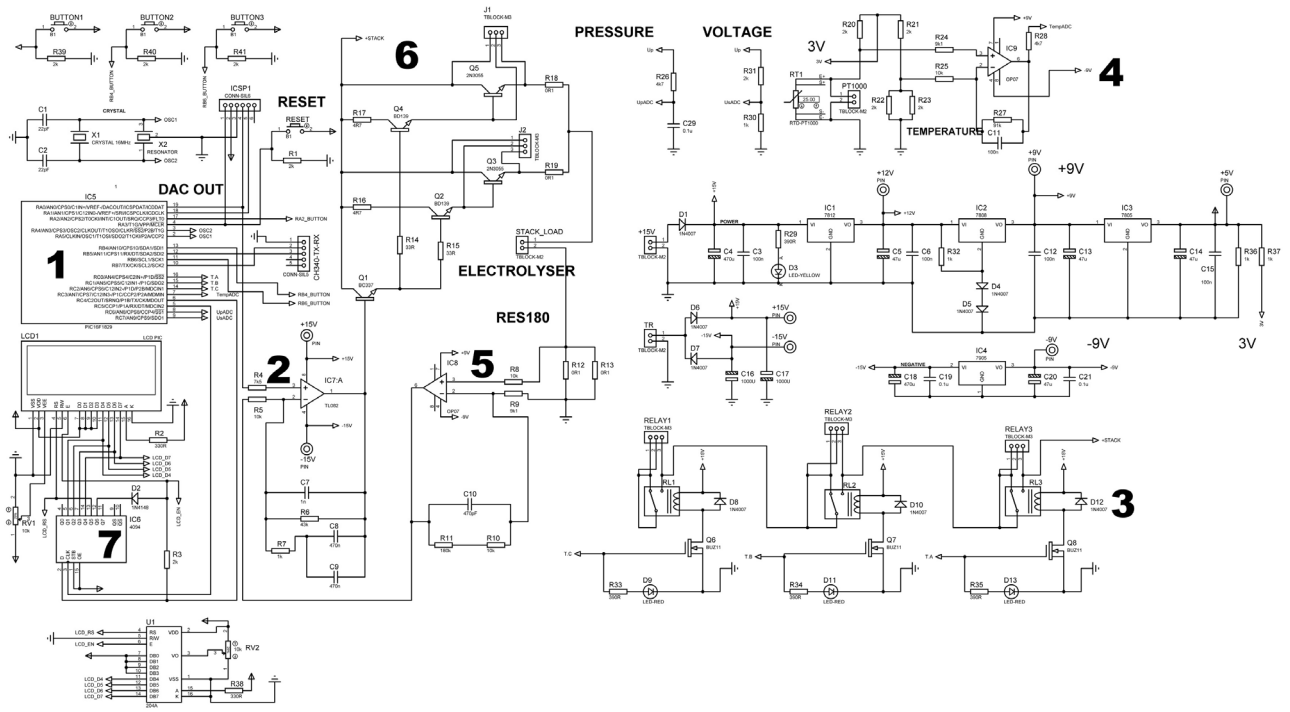

Fig. 2. Schematic diagram of the current regulator.

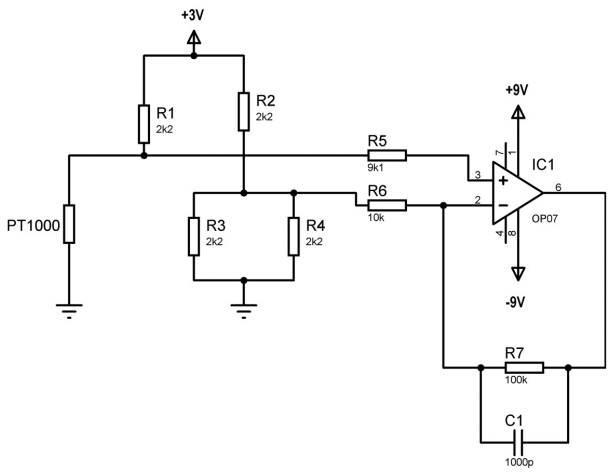

Fig. 3. Schematic of RTD for temperature measurement of electrolyser.

$$\Delta = 533 - 86 = 447\ steps, \tag{2}$$

yielding a coefficient for temperature scaling as follows: 0 steps = 0°C, 447 steps = 100°C. To enable decimal precision, 100 is adjusted to 1000. This resulted in a coefficient of 2.23.

To describe the linear change in temperature, Eq. (3) is used:

$$T°C = \left[\left((0 \div 1023\ steps) * 0.75\right) - 86\ steps\right], \tag{3}$$

where 0.75 is an experimentally taken correction coefficient because the step values for a given temperature may not always be integers, which contributes to measurement error.

Threshold isobaric switch is considered for protection in the event of inadmissible increase in pressure in the system. ABPMANV060PGAA5 pressure sensor with control value range 0 ≈ 60 psi (4.13 bars), analog interface and supply voltage 5 VDC is chosen. Protection has also been added in case of unacceptable increase in the voltage of the electrolysis cell, i.e. upon leaving the regulated potential window, using voltage divider approach (calculated for 12 V).

The construction of all protections is identical, and each one is controlled by the MCU, controlling a relay (RAS1215). All relays are connected in series using a normally open contact. The relay protection circuit thus described is connected in series to the load circuit of the electrolysis cell. Thus, in the event of any emergency, the power circuit mechanically breaks down. In addition, if one of the protection modules fails for some reason, the circuit supplying the electrolysis cell also breaks

down, because normally open contacts are used when the relay is de-energized, regardless of the reason, the circuit breaks.

The software that determines at which moment to turn on or off a given relay takes as a basis the measurements of the ADC unit and the operator settings of which values of the measurements to turn on or off the relays individually. When a value reaches the set by the operator, the processor sends a signal to the relay to turn on or off.

To prevent overloading the controller ports, the circuit incorporates a transistor switch that regulates the current flow through the relay core. Reverse diodes are also provided in the circuit to protect the transistors from switching overvoltages generated when the relay coil is switched because of its inductance.

In the event of a corresponding emergency, the controller deactivates the associated controlled relay and illuminates an LED indicator.

ADC

ADC's receive a signal from the sensors for cell voltage, temperature, and pressure. The calculation of the measured values is done based on arithmetic mean calculations. For this purpose, each of the ADC channels is measured 8 times per unit of time and then the summed result is divided by the number of measurements. In this way, a sufficiently correct result is achieved, because the error accumulated by noises in the supplied voltage and cable lines supplying the signal to the ADC is reduced.

Measuring amplifier

The signal proportional to the current flowing through the electrolysis cell is obtained as a voltage drop across a reference resistance realized with the parallel connected resistors (R_{12} and R_{13} on Fig. 2). Subsequently, the signal proportional to the load current is amplified by an instrumental operational amplifier. A schematic diagram of a non-inverting amplifier is selected.

Output amplifier

The load current is controlled by means of an output amplifier. A Darlington schematic is attached.

LCD display (AMC2004AR-B-B6WTDW)

Standard liquid crystal display, with a size of 20 characters per line (4 lines total) for visualizing data is included. LCD is connected to the MCU via 74HC4094 shift register to reduce the number of display control pins required.

The controller has 4 buttons (RESET, BUTTON1, BUTTON2, and BUTTON3, as shown in Fig. 2) to access various menus and functions of the controller for setting various parameters in the work process. The menus created in the processor software enable the selection of different operating modes of the electrolysis cell, and within a given menu, one or more parameters can be configured. The processor implements the new settings and monitors the operation of the entire installation on the LCD to ensure compliance with the updated configurations. The RESET button is intended for the initial reset of the processor.

Data logging system

An additional feature is the integrated management system for the real time transmission of data acquired from the sensors, along with the relay protection system status, individually to a Windows 10 program (created in C# programming language) executed on a computer system (Fig. 4). This functionality is achieved by using the RS-232 serial communication module within the PIC processor, facilitating the smooth data transmission to the computer program. The program could save the captured data in a text file, which makes the data relevant for processing in graphics software.

The hardware module for serial communication (serial port) is a data shift register (bytes) set to transmit and receive data at a certain standard frequency with a connection to another receiver/transmitter. RS-232 serial port with a standard baud rate setting of 9600 bps is used, with a receiver (Desktop PC) also waiting for data to arrive from another transmitter (PIC16F1829) at the same frequency. The first byte of the transfer means that it contains the temperature value and will be displayed in the temperature field ADC1 (pressure - ADC2, cell voltage - ADC3). The second, third and fourth bytes are the states of the relays for each separately. If the byte value is equal to 1, the corresponding relay is on, if it is equal to 0, the relay is off. Each relay has a separate label that shows the status of each relay individually as well as other data for managing the controller.

Dynamic current profileh

In additional experimental research, the differences

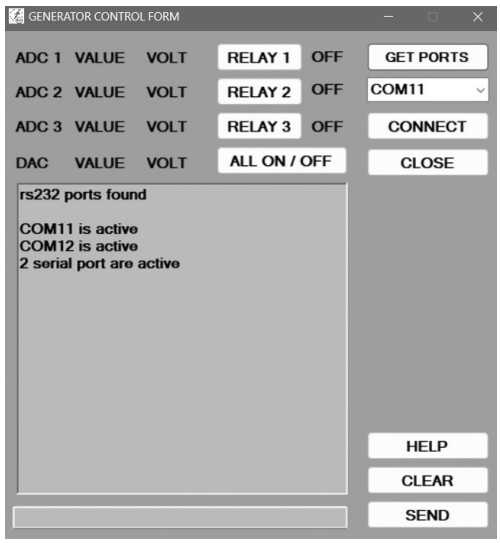

Fig. 4. RS-232 graphical user interface (GUI) for the current regulator.

in current and voltage responses to step inputs in electrochemical systems were analysed. It was observed that a step current input induces an abrupt change in the capacitive current, while the Faradic current remains unaffected at both the anode and the cathode. Conversely, a voltage step input generates a non-monotonic current response characterized by in initial decline followed by a subsequent increase, a phenomenon referred to as "overshoot". This overshoot occurs exclusively during rapid voltage transitions. Furthermore, the current response to a voltage step is significantly faster than the voltage response to a current step, as noted in [12]. These observations underscore the necessity of incorporating capabilities for conducting pulse testing.

In related experimental studies investigating the initiation of H_2 production, it was observed that the voltage remained below the threshold required to start the reaction. The key factor influencing this was the duty cycle, which is defined as the fraction of a signal or system's period during which it is active. When the duty cycle falls below 50 %, the effective voltage fails to reach the necessary level to trigger the reaction. At these lower duty cycle values, no H_2 production was detected in experiments, indicating insufficient input energy. To ensure the effective initiation of the reaction, the duty cycle was adjusted to a maximum of 80 %, constrained by the limitations of the signal generator used (GWINSTEK GFG-8219A). This setting allows the voltage to exceed the threshold necessary for triggering the reaction, thereby supporting successful H_2 production under controlled conditions [13].

To address this limitation, improvements were implemented in the management and power module of the system, enabling the variation of the duty cycle up to 100 % in the circuit described in [13]. A programmable signal generator, specifically designed for electrolysis testing, was incorporated in place of the external functional generator. This enhancement allows the system to operate effectively even in non-laboratory environments, thereby increasing its practicality for broader applications.

Square wave tests were conducted at frequencies of 100mHz and 1Hz, following the algorithm outlined in [12 - 15] on a commercial electrolysis cell [16]. This work explores enhancing the efficiency of electrolytic cell by applying a modulated square signal to the current. By adding an alternating current to the DC component in the electrolysis cell, the detachment of gas bubbles from the electrode can be facilitated, reducing the insulating effect of gas on the electrolyte-electrode interface and improving overall performance.

For the task, a schematic diagram for the functional generator was developed, shown on Fig. 5.

PIC18F46K20 processor was utilized, featuring a maximum operating speed of 64 MHz, 4 KB RAM, 64 KB flash memory, and 1KB EEPROM. The processor can operate with a quartz crystal or resonator up to 16 MHz, reaching the maximum frequency through its internal programmable frequency multiplier (PLL). The trimmer potentiometer labelled "TRIMER1" on Fig. 5 controls the analog function (PWM variable).

For time indication, the "Indication" module is utilizing "LED3" led diode.

PWM functionality is implemented via the Timer0 module (pin 39 - RB6) [17], which actively manages PWM signals while Timer0 is active [17]. A continuous check within an "if" condition ensures Timer0 remains active (set to 1) until the specified end time (Timer2) is reached, at which point Timer0 resets to 0. This approach provides precise control over the output signal, aligning with top-down programming logic for optimal clarity and operational stability.

To facilitate stable PWM operation, Timer2 serves as the secondary timer. Achieving low frequencies required an additional software frequency divider (counter), because timer modules are hardware restricted by the

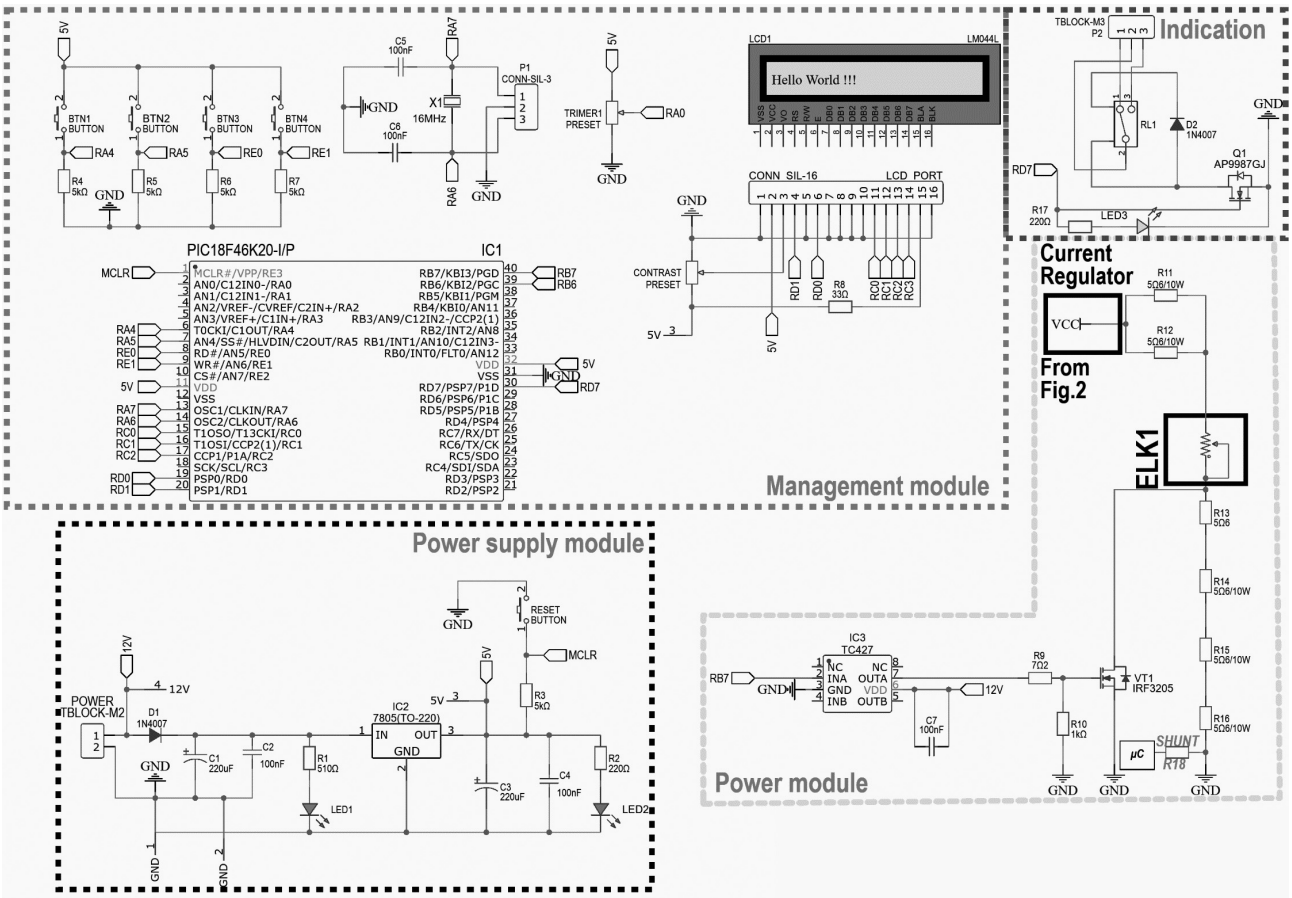

Fig. 5. Electrolysis cell pulse control.

quartz crystal and the registers intended for frequency division.

The schematic works on the following principle illustrated in Fig. 5. When the supply voltage is activated, current flows through the circuit, originating from the current regulator (described in previous section). The path includes the supply voltage, resistors R_{11}, R_{12}, electrolysis cell ElK1, resistors R_{13}, R_{14}, R_{15}, R_{16}, and ground.

In practice, the cumulative resistance of the components R_{11}, R_{12}, R_{13}, R_{14}, R_{15}, and R_{16} determines the value of the free, or independent, DC component. This relationship is mathematically expressed in Eq. (4):

$$I_0 = \frac{U_p - U_{ELK}}{\frac{R_{11}.R_{12}}{R_{11}+R_{12}} + R_{13} + R_{14} + R_{15} + R_{16}}, \quad (4)$$

where: I_0 - value of the independent component of the direct current, U_p - value of the power supply voltage, U_{ElK} - voltage drop across the electrolysis cell.

In practice, the transistor Q_1 plays the role of a switch. During its saturation, resistors R_{13}, R_{14}, R_{15}, and R_{16} are shunted. In this situation, Eq. (4) takes the form shown in Eq. (5):

$$I_m = \frac{U_p - U_{ELK}}{\frac{R_{11}.R_{12}}{R_{11}+R_{12}} + R_{SD}}, \quad (5)$$

where: R_S is the source-drain resistance of the transistor in saturated state, which for the chosen type of transistor is 8 mΩ and can be neglected. In other words, the current will be limited by the parallel connected resistors R_{11} and R_{12} and the internal resistance of the cell. To achieve higher manufacturability of the project, the value of all resistors is chosen to be the same (5.6 Ω). If a comparison is made between the independent component of the current and its pulse value, it can be written as shown in Eq. (6):

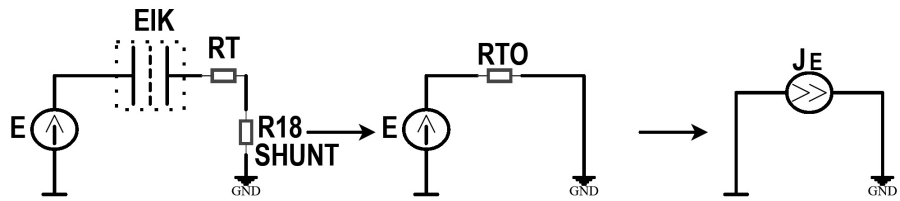

Fig. 6. Equivalent schematic of the power module from the electrolysis cell pulse control setup.

$$S = \frac{\frac{R_{11}.R_{12}}{R_{11}+R_{12}} + R_{13} + R_{14} + R_{15} + R_{16}}{\frac{R_{11}.R_{12}}{R_{11}+R_{12}}}, \quad (6)$$

From Eq. (6) it is easy to see that the ratio in the equation S = 9 times, assuming all resistors are the same.

The equivalent schematic of the power module from Fig. 5 is given on Fig. 6. This representation simplifies the original circuit, focusing on the essential components and their interconnections within the power module to facilitate analysis and understanding of its operation. The equivalent schematic highlights the critical parts for current flow and voltage regulation, as well as the relationship between the supply voltage, resistive elements, and the electrolysis cell.

The limiting current is determined from Eq. (7):

$$J_E = \frac{E}{R_{TO}}, \quad (7)$$

where J_E is the current flowing through the electrolysis cell, E is the applied cell voltage, and R_{TO} is the current limiting resistor (equivalent resistance of R_{13}, R_{14}, R_{15}, and R_{16}).

A programmable shunt resistor (R_{18} shown in Fig. 5) has been integrated into the system to measure the current passing through the electrolysis cell. This resistor is capable of operating over a wide range, from 3 nA to 3 A, enabling precise measurements across different current levels. The corresponding schematic is illustrated in Fig. 7. Measuring current in the nanoampere range requires the use of high-value resistors to mitigate the effects of the input offset current and offset voltage of the operational amplifier, as outlined in [18]. The input offset currents typically fall within the range of 10 pA to 50 nA, while the offset voltages are in the microvolt range. These characteristics necessitate the selection of resistors with sufficiently high values to ensure accurate current measurement and minimize errors introduced by the amplifier's inherent properties.

To achieve a measurable current of 3 nA, a minimum input voltage of 10 mV is required at the processor. This necessitates the use of a 3.3 MΩ resistor to ensure the appropriate voltage drop. The OPA333AIDBV precision operational amplifier was selected for buffering, owing to its low offset voltage and high accuracy. With an overall system gain of 5000, the equivalent shunt resistor value was calculated to be 666.6 Ω (560 Ω standard value).

A PIC16F1827 MCU was employed to measure the amplified voltage output from the operational amplifier and to manage range switching through relays. The measured current values are displayed in real-time on an alphanumeric LCD (AC-162BYILY-H), providing clear and precise feedback for monitoring the system's performance. This configuration ensures high sensitivity and accuracy across a wide range of currents.

The shunt design is powered by a 5 V supply connected to the PIC16F1827 MCU and utilizes a 10-bit ADC. This configuration provides ADC resolution of 4.88 mV per step. As a result, to accurately measure a current of 3 nA, the system requires a minimum input voltage of 10 mV, equivalent to slightly more than two ADC steps, ensuring sufficient precision for low-current measurements. Under this configuration, the full-scale voltage of 5 V corresponds to a maximum measurable current of 1.5 mA. This design allows for reliable current measurements across a wide dynamic range, while maintaining adequate resolution for both low and high current values. With a shunt resistor value of 560 Ω, the output of integrated circuit (IC) *U2* measures a maximum current of 0.595 mA, resulting in a voltage of 5 V at point "*I_max*" (Fig. 5). The output of *U4* registers a minimum current of 3 nA, generating a voltage of 11.11 mV. When the shunt resistor value is 0.1 Ω, the output

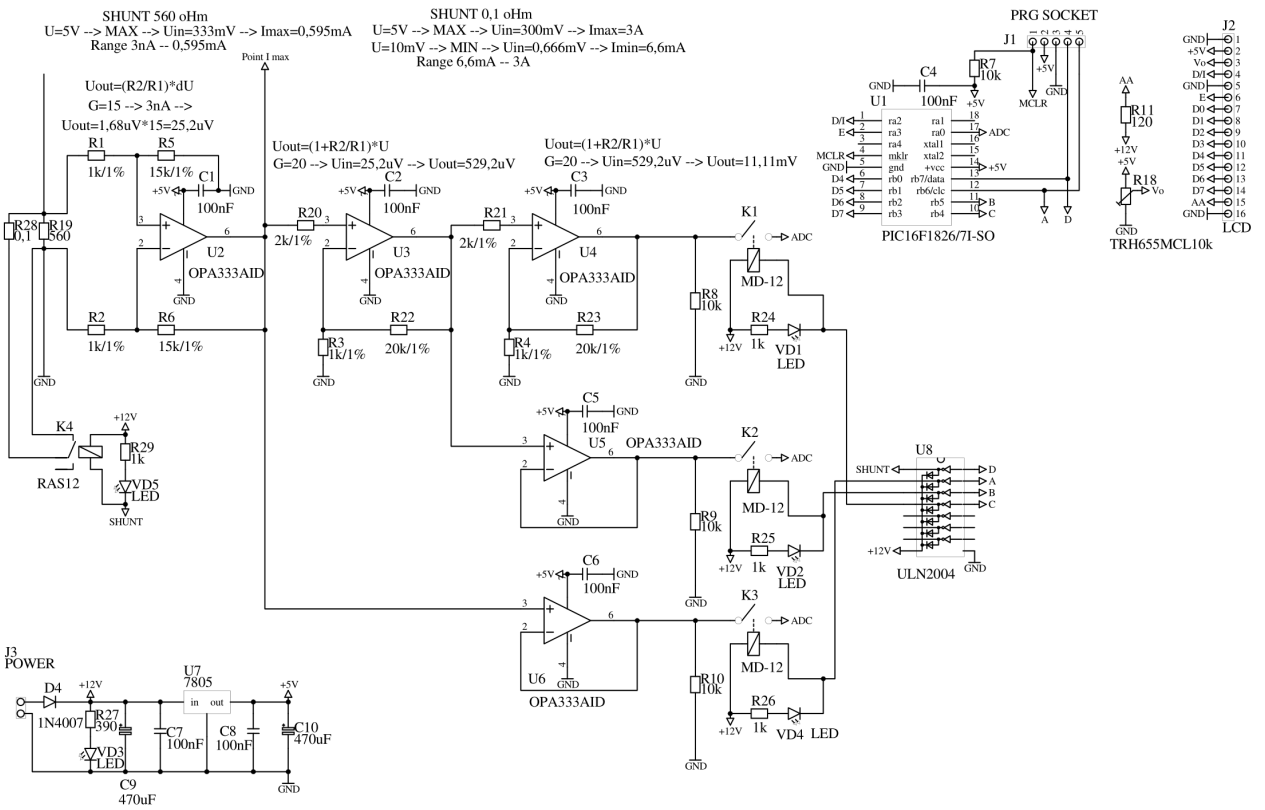

Fig. 7. Programmable shunt resistor for electrolysis cell pulse control setup.

of *U2* measures a maximum current of 3 A, producing a voltage of 4.5 V at point "*I_max*" (Fig. 5). For a current of 6.6 mA at *U2*, the corresponding output voltages are 10 mV at *U2*, 100 mV at *U3*, and 1 V at *U4*. The entire range can be covered from 0.6 mA, where *U3* registers 10 mV, and *U4* - 100 mV.

RESULTS AND DISCUSSION

The current regulator utilized for the experiments is illustrated in Fig. 8a. In constant power load mode, the performance of the commercial electrolysis cell was evaluated by applying varying current levels over identical time intervals. The obtained experimental data are summarized in Tables 1 - 4. The relationship between the cell voltage, the cell temperature and the applied current, recorded at 30-min intervals, is depicted in Fig. 9a. This analysis highlights the thermal response of the electrolysis cell under different current loads, providing insight into the thermal management requirements and efficiency of the system during operation.

Tables 5 and 6 refer to the applied pulse mode at frequencies of 100 mHz and 1 Hz, comparing the deviation of cell voltage and temperature with those in the DC operation mode.

The PWM generator used in the system is illustrated in Fig. 8b. Under both operational modes, the average current passing through the electrolysis cell is approximately 790 mA. The comparative analysis of the effects of current frequency on cell voltage is presented in Fig. 9c, which shows the cell voltage under three distinct modes: constant current and pulsed current at two different frequencies.

Additionally, the impact of pulse load on the cell temperature is depicted in Fig. 9d. This study was conducted for the same average current of 790 mA across three operating modes: constant current and pulsed current at two different frequencies. The results provide insights into the thermal behaviour and efficiency of the electrolysis cell under varying current profiles, highlighting the influence of frequency on both voltage stability and thermal management.

Fig. 9b illustrates that the cell voltage increases consistently under a constant current of 1.1 A for a duration of 120 min. This phenomenon has also been reported in previous studies [10, 19, 20]. The increase in cell voltage over time can be attributed to several factors, including the growing polarization of the electrodes, the degradation of the PEM, and the accumulation of reaction byproducts. Collectively, these factors contribute to higher internal resistance within the PEM electrolysis cell, as discussed in [21].

Table 1. 344 mA load current.

Time, min	Cell current, mA	Temperature, °C	Cell voltage, V
0	344	23.2	1.85
30	344	23	1.86
60	344	23	1.86
90	344	23	1.86
120	344	23	1.86

Table 2. 700 mA load current.

Time, min	Cell current, mA	Temperature, °C	Cell voltage, V
0	700	24	2.01
30	702	24.4	1.99
60	703	24.4	1.99
90	703	24.4	1.99
120	703	25.1	1.99

Table 3. 940 mA load current.

Time, min	Cell current, mA	Temperature, °C	Cell voltage, V
0	940	24.4	2.07
30	941	24.8	2.06
60	942	24.8	2.05
90	941	24.8	2.06
120	941	25.4	2.06

Table 4. 1108 mA load current.

Time, min	Cell current (mA)	Temperature, °C	Cell voltage, V
0	1108	22.2	2.09
30	1195	22.6	2.1
60	1272	23	2.11
90	1260	23	2.11
120	1328	23	2.16

Table 5. Pulse load, 100 mHz.

Time, min	Cell current, A	Temperature, °C	Cell voltage, V
0	1.645	24	2.693
30	1.558	24.4	2.546
60	1.474	24.4	2.453
90	1.389	24.6	2.357
120	1.218	24.6	2.212

Table 6. Pulse load, 1 Hz.

Time, min	Cell current, mA	Temperature, °C	Cell voltage, V
0	1.59	22.2	2.629
30	1.53	22.6	2.525
60	1.49	23	2.463
90	1.38	23	2.331
120	1.24	23	2.259

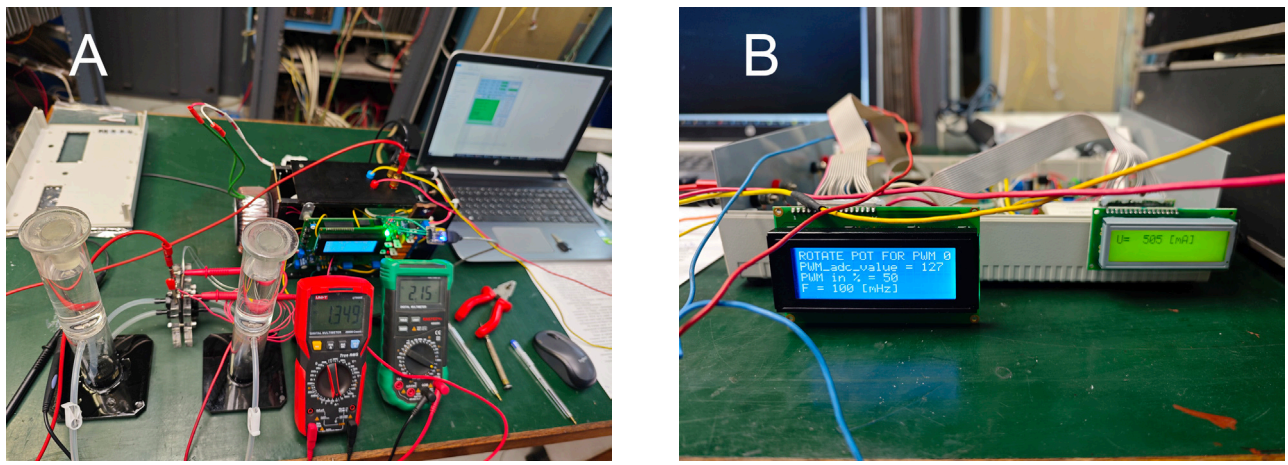

Fig. 8. (A) Module for controlling and stabilizing the current through the electrolysis cell, (B) pulse control electrolysis setup

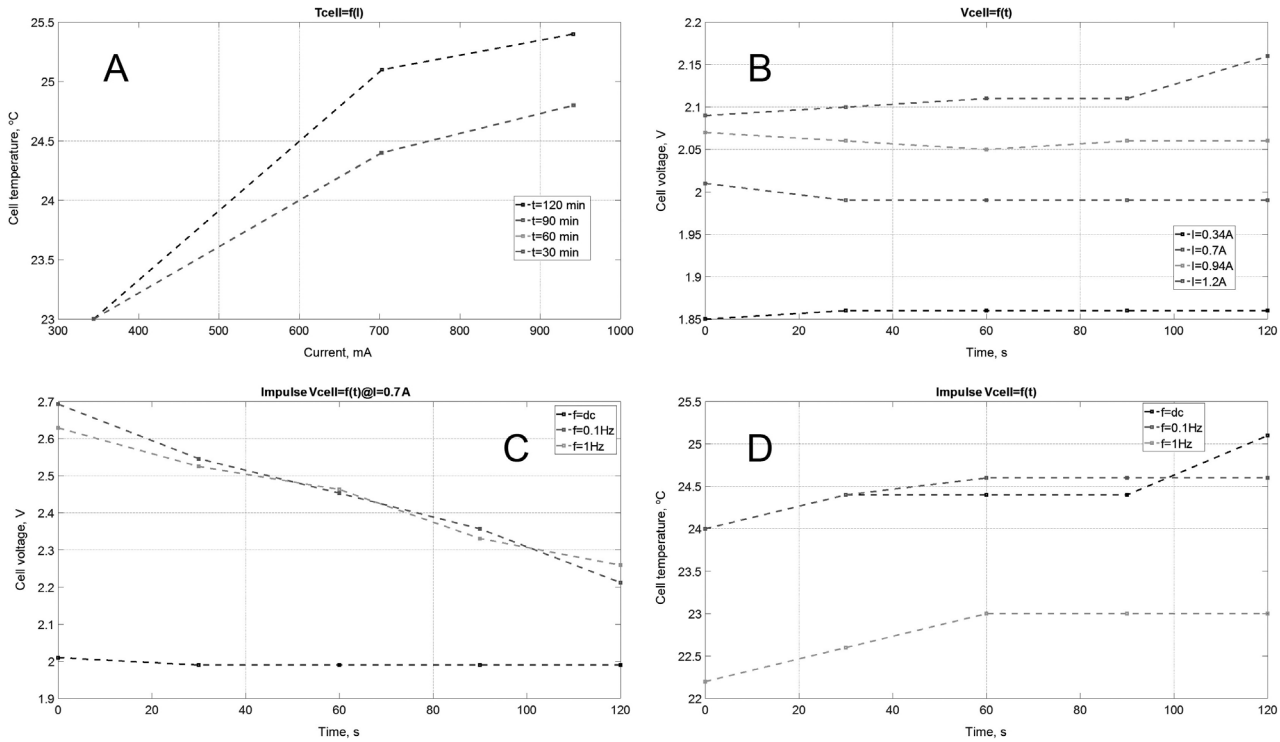

Fig. 9. Measurements obtained from the current regulator: (a) Electrolysis cell temperature dependence on current load; (b) Electrolysis cell voltage dependence on time; (c) Pulse electrolysis cell voltage dependence on time; (d) Pulse electrolysis temperature dependence on time.

The increased resistance necessitates a higher voltage for the electrolysis process, thereby reducing the system's overall efficiency. Furthermore, this effect is exacerbated by high current densities (depicted by the purple curve) and extended periods of operation, which accelerate membrane degradation and amplify electrode polarization.

Fig. 9c demonstrates that, under pulsed current loading, the cell voltage decreases over time, in contrast to the behaviour observed under constant current conditions. The reduction in cell voltage during pulsed operation can be explained by several mechanisms. The recovery periods between pulses mitigate polarization resistance and reduce the accumulation of bubbles on the electrode surfaces. Additionally, pulsed loading minimizes system heating, thereby preventing temperature-induced increases in resistance. The transient nature of the current pulses also modifies reaction kinetics, promoting more efficient electrochemical reactions, as corroborated in [22]. In contrast, continuous DC operation results in sustained polarization resistance, continuous heating, and less efficient reaction rates, which collectively lead to a higher cell voltage, as depicted in Fig. 9B (purple curve). These findings align with the experimental observations reported by Vincent et al., which demonstrated that at higher pulse frequencies, the shortened pulse duration prevents the electrodynamic diffusion layer from reaching a steady state thickness [23]. This interruption allows reacting ions to return to the electrode surface, restoring the surface concentration to its original value before the next pulse. Consequently, the overall cell voltage is reduced. The study concludes that the thickness of the electrodynamic diffusion layer is proportional to the pulse duration.

Fig. 9d indicates that the temperature increases at higher pulse frequencies for a given average current through the cell. Recovery periods between current pulses reduce polarization resistance by facilitating the detachment of gas bubbles, thereby lowering overpotential [24]. Furthermore, reduced heating during off-periods limits temperature increases, minimizing thermal degradation and preserving ionic conductivity within the PEM electrolysis cell. The periodic

interruptions in current flow also alter electrochemical reaction kinetics, enhancing reaction efficiency and reducing overpotentials. The overall ohmic losses are diminished due to the less continuous nature of the current flow, resulting in more stable thermal conditions. Experimental results at 80°C reveal that the cell voltage in the PEM electrolyser is influenced by a combination of reversible voltage, activation overvoltage, and ohmic overvoltage. Higher temperatures were observed to decrease the cell voltage, whereas lower temperatures increased it, regardless of the scenarios involving step currents, as reported in [10].

CONCLUSIONS

Continuous DC operation results in elevated polarization resistance, sustained heating, less efficient reaction kinetics, and increased ohmic losses. These factors collectively necessitate a higher cell voltage for the electrolysis process. Consequently, pulse loading provides a significant advantage by reducing the voltage required to sustain electrolysis and enhancing the overall efficiency of the system. Experimental findings indicate that a pulse current frequency of 1 Hz with a 50 % duty cycle represents a stable and effective operating mode.

Modern control systems have been developed to manage the electrochemical processes in PEM electrolysers. These systems utilize potentiostatic device, which function as power supplies to regulate current, monitor cell voltage, and track operational parameters such as temperature and gas pressure. By integrating a PWM frequency generator, a pulse electrolysis mode can be implemented. Laboratory-validated operating regime can be programmed into these control systems, ensuring that PEM electrolysers perform optimally under real operating conditions.

Acknowledgments

The authors kindly acknowledge the financial support of project № BG05M2OP001-1.002-0014 "Center of competence HITMOBIL - Technologies and systems for generation, storage and consumption of clean energy, funded by Operational Programme "Science and Education For Smart Growth" 2014-2020, co-funded by the EU from European Regional Development Fund.

Authors' contributions: *J.I. performed all experimental work, including the design and implementation of the electronic system for powering and controlling the electrolysis cell. D.B. assisted with the calculations for block 2 (Fig. 2). G.B. supported the preparation of the mechanical structure housing the DC regulator. V.D. calibrated the temperature sensor (Fig. 3) and set up the serial communication (Fig. 4). E.S. provided methodological guidance and contributed to the analysis and interpretation of the results.*

REFERENCES

1. https://www.fuelcellstore.com Accessed: Apr. 14, 2025. [Online]
2. S. Toghyani, S. Fakhradini, E. Biniasadi, M.Y. Abdollahzadeh, M. Safdari Shadloo, Optimization of operating parameters of a polymer exchange membrane electrolyzer, International Journal of Hydrogen Energy, 44, 13, 2019, 6403-6414.
3. L.M. Gandia, G. Arzamendi, P.M. Dieguez, Renewable hydrogen technologies, Amsterdam, 2013.
4. J. Koponen, A. Kosonen, V. Ruuskanen, K. Huoman, M. Niemela, J. Ahola, Control and energy efficiency of PEM water electrolyzers in renewable energy systems, International Journal of Hydrogen Energy, 42, 50, 2017, 29648-29660.
5. M. Carmo, D.L. Fritz, J. Mergel, D. Stolten, A comprehensive review on PEM water electrolysis, International Journal of Hydrogen Energy, 38 ,12, 2013, 4901-4934.
6. R.E. Clarke, S. Giddey, F.T. Ciacchi, S.P.S. Badwal, B. Paul, J. Andrews, Direct coupling of an electrolyser to a solar PV system for generating hydrogen, International Journal of Hydrogen Energy, 34, 12, 2009, 2531-2542.
7. R.E. Clarke, S. Giddey, S.P.S. Badwal, Stand-alone PEM water electrolysis system for fail safe operation with a renewable energy source, International Journal of Hydrogen Energy, 35, 3, 2010, 928-935.
8. H. Sayed-Ahmed, A.I. Toldy, A. Santasalo-Aarnio, Dynamic operation of proton exchange membrane electrolyzers degradation - critical review, Renewable and Sustainable Energy Reviews, 189, 2024, 113883.

9. A.Z. Tomic, I. Pivac, F. Barbir, A review of testing procedures for proton exchange membrane electrolyzer degradation, Jornal of Power Sources, 557, 2023, 232569.
10. C. Rakousky, U. Reimer, K. Wippermann, S. Kuhri, M. Carmo, W. Lueke, D. Stolten, Polymer electrolyte membrane water electrolysis: Restraining degradation in the presence of fluctuating power, Journal of Power Sources, 342, 2017, 38-47.
11. Microchip Technology, "PIC16f1829," Accessed: Apr. 14, 2025. [Online]. Available: https://www.microchip.com/en-us/product/pic16f1829.
12. J. Dang, F. Yang, Y. Li, X. Deng, M. Ouyang, Transient behaviors and mathematical model of proton exchange membrane electrolyzer, Journal of Power Sources, 542, 2022, 231757.
13. N.C. Ereli, M. Kisti, T. Esiyok, E. Ozdogan, B. Huner, N. Demir, M.F. Kaya, First pulsed control system design for enhanced hydrogen production performance in proton exchange membrane water electrolyzers, Fuel, 371, 2024, 132027.
14. H.P.C. Buitendach, R. Gouws, C.A. Martinson, C. Minnaar, D. Bessarabov, Effect of ripple current on the efficiency of a PEM electrolyser, Results in engineering, 10, 2021, 100216.
15. Z. Dobo, A.B. Palotas, Impact of the current fluctuation on the efficiency of Alkaline Water Electrolysis, International Journal of Hydrogen Energy,42,9, 2017, 5649-5656.
16. FuelCell Store, "1-Cell Rebuildable PEM Electrolyzer Kit", Accessed: Apr. 14, 2025. [Online]. Available: https://www.fuelcellstore.com/1-cell-rebuildable-pem-electrolyzer-kit-htec-e208.
17. Microchip Technology, "PIC18f46k20," Accessed: Apr. 14, 2025. [Online]. Available: https://www.microchip.com/en-us/product/pic18f46k20.
18. PalmSens4, "Potentiostat Fundamentals," Accessed: Apr. 14, 2025. [Online]. Available: https://www.gamry.com/application-notes/instrumentation/potentiostat-fundamentals/.
19. K.W. Ahmed, M.J. Jang, M.G. Park, Z. Chen, M. Fowler, Effect of Components and Operating Conditions on the Performance of PEM Electrolyzers: A Review, Electrochem, 3, 4, 2022, 581-612.
20. C. Rakousky, U. Reimer, K. Wippermann, M. Carmo, W. Lueke, D. Stolten, An analysis of degradation phenomena in polymer electrolyte membrane, Journal of power sources, 326, 2016, 120-128.
21. S.H. Frensch, F. Fouda-Onana, G. Serre, D. Thoby, S.S. Araya, S.K. Kaer, Influence of the operation mode on PEM water electrolysis degradation, International Journal of Hydrogen Energy, 44, 57, 2019, 29889-29898.
22. F. Mustapha, D. Guilbert, M. El-Ganaoui, Investigation of Electrical and Thermal Performance of a Commercial PEM Electrolyzer under Dynamic Solicitations, Clean Technologies, 4, 4, 2022, 931-941.
23. I. Vincent, B. Choi, M. Nakoji, M. Ishizuka, K. Tsutsumi, A. Tsutsumi, Pulsed current water splitting electrochemical cycle for hydrogen production, International Journal of Hydrogen Energy, 43, 22, 2018, 10240-10248.
24. X. Su, L. Xu, B. Hu, Simulation of proton exchange membrane electrolyzer: Influence of bubble covering, International Journal of Hydrogen Energy, 47, 46, 2022, 20027-20039.